ICCFD13 MILAN ITALY 2026

Simulation of Unsteady Turbulent Flows over the Caradonna-Tung Rotor with SU2

S. Soğancı[*,**] and İsmail H. Tuncer[**]
[*] Turkish Aerospace, Türkiye
[**] Aerospace Engineering Department, Middle East Technical University, Türkiye
Corresponding author: semih.soganci@tai.com.tr

This study presents a numerical investigation of unsteady flow fields surrounding the Caradonna-Tung rotor, serving as a critical validation baseline for rotorcraft aerodynamic simulations. Utilizing an experimental test case [1] at 1500 RPM and an 8° collective pitch, the research employs a multi-block grid structure framework integrated with a sliding interface to resolve the unsteady transient rotational flow physics. The numerical results demonstrate a strong correlation with experimental surface pressure distributions (C_p) and thrust coefficient (C_T), confirming the accuracy of the unsteady flow solver and the effectiveness of the grid structure. The study provides the necessary foundation for future high-fidelity studies involving fully coupled fluid-structure interaction (FSI) and the implementation of deforming mesh blocks for comprehensive aeroelastic analysis.

Keywords: Reynolds Averaged Navier-Stokes, Block Mesh Structure, Sliding Interface

1. Introduction

The aerodynamic and structural design of helicopter main rotor systems remains one of the most formidable challenges in aerospace engineering. Because rotor blades operate under highly dynamic, asymmetric, and time-varying flowfields, they are subjected to severe cyclic aerodynamic loads, structural vibrations, and complex aeroelastic couplings [2]. Structural failures in these rotating components are frequently catastrophic, making the high-fidelity prediction of vibratory loads and aerodynamic forces essential not only for structural integrity and flight safety but also for accurate fatigue life estimation and component certification [3]. Rotary-wing blades are inherently characterized by high aspect ratios, rendering them susceptible to substantial elastic deflections under operational loads. These deformations encompass complex, coupled flap, lead-lag, and torsional (feathering) degrees of freedom that alter the local effective angle of attack, establishing a highly non-linear feedback loop between the surrounding fluid and the structural response [4]. Consequently, capturing these complex interactions demands robust and sophisticated aeroelastic analysis frameworks throughout the design and optimization phases.

In contemporary industry practice, aeromechanical and aeroelastic behaviors are conventionally predicted using Comprehensive Analysis (CA) codes, such as Dymore [5] or CAMRAD [6]. These structural dynamics environments typically model the rotor blade assembly as an arrangement of flexible, one-dimensional beams or multi-body joints coupled with low-order aerodynamic representations, such as Lifting Line Theory (LLT) or lifting surface methods supplemented by empirical dynamic stall formulations [7]. While these semi-empirical comprehensive models are computationally efficient and highly effective for initial design sweeps and performance trends, they exhibit intrinsic limitations when encountering highly non-linear, multi-dimensional flow phenomena. Specifically, low-order aerodynamic methods struggle to accurately capture localized three-dimensional effects, transonic shock wave/boundary-layer interactions at the advancing blade tip, deep dynamic stall, and complex Blade-Vortex Interactions (BVI) where a blade collides with the concentrated tip vortices shed by preceding blades [8]. To overcome these aerodynamic deficiencies without sacrificing structural fidelity, the paradigm in state-of-the-art rotorcraft research has progressively shifted toward coupled Computational Fluid Dynamics and Compu-

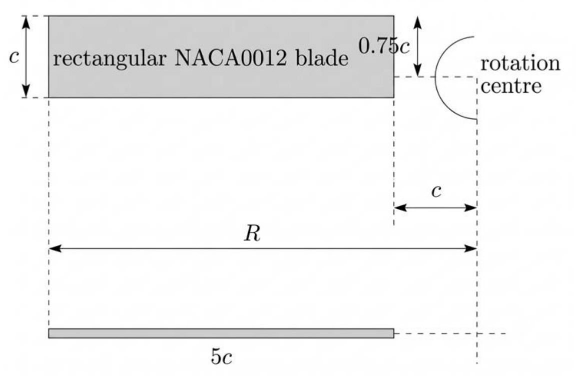

Figure 1: Caradonna-Tung Rotor Model [16]

Table 1: Operating and geometric parameters for the Caradonna-Tung rotor test case (1,500 RPM, 8° collective) [1, 16].

Number of blades	2
Roor radius	1.143 m
Blade chord	0.1905 m
Rotor speed	1500 rpm
Collective angle	8°
Airfoil profile	NACA 0012
Tip Mach number (M_{tip})	0.5262
Tip Reynolds number (Re_{tip})	2 316 500

tational Structural Dynamics (CFD-CSD) frameworks [9, 10]. This multi-disciplinary coupling integrates high-fidelity, Navier-Stokes flow solvers with advanced structural dynamic codes to accurately capture non-linear, deterministic aerodynamic forces, facilitating a rigorous analysis pathway toward virtual certification.

As a critical, foundational milestone toward building a fully coupled aeroelastic framework, the present study conducts high-fidelity numerical investigations of the two-bladed Caradonna-Tung rotor in an isolated hover state [8]. Simulations are carried out under demanding operational conditions at a rotational speed of 1500 RPM and a collective pitch angle of $\theta_0 = 8°$, which introduces pronounced three-dimensional tip effects and strong vortex development. In this initial phase, a rigid-blade formulation is intentionally enforced to systematically isolate the flow solver from structural feedback loops. Spatial discretization is achieved via a multi-block hybrid grid configuration meticulously engineered in Pointwise, providing an adaptable topological foundation designed to seamlessly incorporate deforming mesh blocks and explicit structural blade motions in subsequent coupling phases. Utilizing the open-source SU2 suite [11] governed by a sliding interface zone, the computational strategy successfully captures the transient development of the wake column and localized vortex dynamics without introducing structural non-linearities. This approach yields a rigorously validated baseline for sectional surface pressure distributions and integrated global thrust coefficients before transitioning to fully coupled Fluid-Structure Interaction (FSI) problems. Finally, the computed unsteady flow fields are processed using the open-source ParaView application to extract precise quantitative surface pressures and track the spatial trajectories of the tip vortices as they propagate downstream into the wake.

2. Methodology

The compressible Navier-Stokes equations are solved within the open-source SU2 suite using the integral form of the conservation laws [11, 12]. To accurately account for viscous effects, the laminar viscosity is modeled as a function of temperature via Sutherland's law, while the one-equation Spalart-Allmaras (S-A) model is utilized to resolve eddy viscosity and turbulence closure near the solid wall boundaries [13]. For spatial discretization, Roe's upwind energy-splitting scheme is applied for the convective flux calculations, coupled with a Monotonic Upstream-centered Scheme for Conservation Laws (MUSCL) approach to ensure second-order spatial accuracy [14]. Unsteady flow physics are captured using the classic dual-time-stepping approach proposed by Jameson [15]. Within each discrete physical time step, 10 pseudo-sub-iterations are performed to ensure convergence of the non-linear residual equations by marching the solution to a steady state in fictitious pseudo-time. Boundary data and conservative flow variables are exchanged across adjacent multi-block grid domains at the termination of every pseudo-iteration using the nearest-neighbor approach through sliding interface. To ensure sufficient temporal resolution of the unsteadiness and wake evolution, the physical time step (Δt) is rigidly constrained to match an azimuthal rotation increment of exactly $\Delta\psi = 2°$ per physical time step.

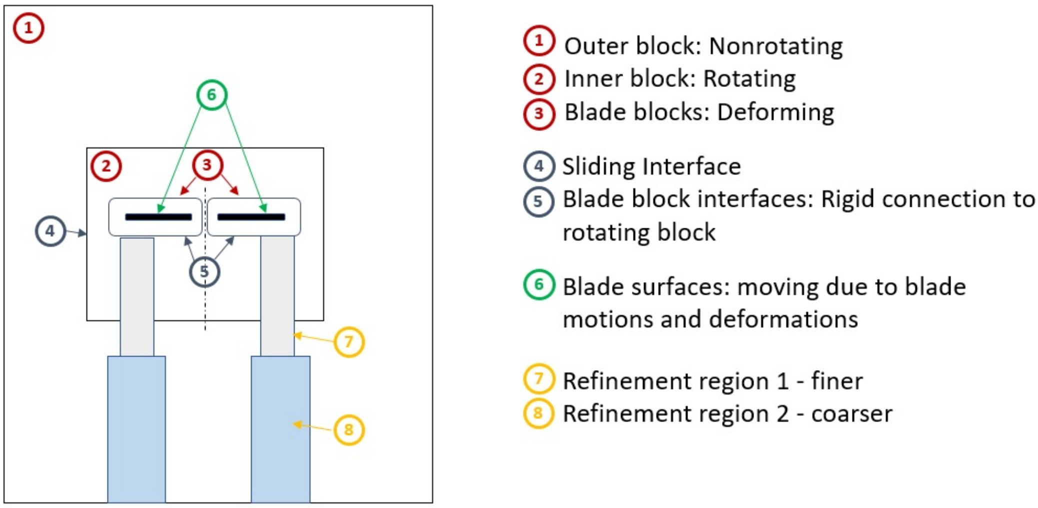

Figure 2: Block Mesh Structure

Block mesh structure is generated in Pointwise and it is given in Figure 2. The computational domain is divided into a stationary outer block (1) for ambient conditions and a rotating inner zone (2) that houses the rotor. These two regions are connected by a sliding interface (4), allowing the rotor rotation. Directly around the blade surfaces (6), specialized near-body blocks (3) are used to handle potential deformations and blade motions. To capture the rotor's wake efficiently, the model uses a nested refinement strategy: a fine mesh zone (7) sits immediately under the rotor to resolve high-velocity gradients, while a coarser zone (8) is used further downstream to track the wake as it dissipates. This approach ensures high accuracy in the flow field without wasting computational power on areas far from the action.

The pressure far-field boundary condition is applied to the top and lateral boundaries to ensure an accurate representation of ambient conditions. The bottom boundary is specified as a pressure outlet, while an adiabatic, no-slip boundary condition is enforced on the blade surfaces. To fully resolve the viscous sublayer, the target y^+ value is kept below 1. Accordingly, the first wall thickness is set to 2×10^{-3} mm (2 μm), utilizing 28 boundary layer cells with a grid stretching ratio of 1.2. An overview of the resulting computational grid is presented in Figure 3.

The multi-block hybrid mesh topologies are partitioned and parallelized using the native Message Passing Interface (MPI) framework of the SU2 suite. Parallel computations are deployed across dedicated compute nodes powered by high-density processors to accelerate residual convergence during the Unsteady pseudo-sub-iterations.

3. Results and Discussion

The induced flowfield is evaluated via the Mach number contours and superimposed streamlines presented in Figure 4. The flow topology exhibits a classic hover profile, characterized by distinct fluid induction from the ambient region above the rotor plane into a high-velocity downward slipstream. The fluid accelerates smoothly over the blade surface, peaking near the tips in alignment with the highest local aerodynamic loading. Beneath the rotor disk, a well-defined contracted wake column forms, maintaining a concentrated core of elevated velocity as it propagates downstream.

The quantitative predictive accuracy of the numerical framework is critically evaluated through the sectional surface pressure coefficient (C_p) distributions presented in Figure 5. The computational predictions for both the coarse and fine meshes are extracted after 20 full blade rotations to ensure that the starting vortex clears the solution domain and a fully developed hover wake is established. The C_p profiles are

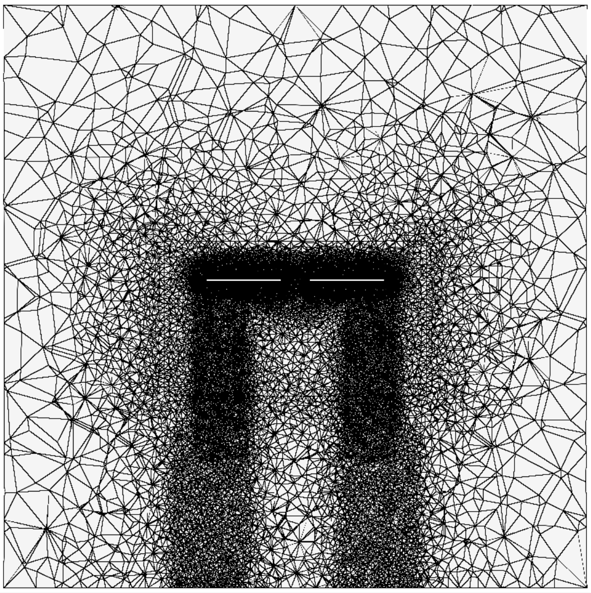

(a) Full Computational Domain Section

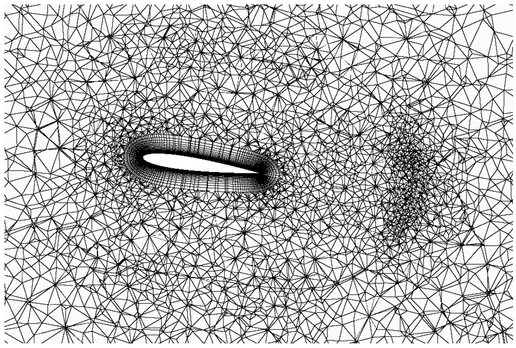

(b) Near-Body Mesh Section ($r/R = 0.5$)

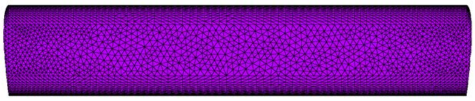

(c) Blade Surface Mesh

Figure 3: Multiblock grid structure

compared against the experimental data across five distinct radial stations ($r/R = 0.50, 0.68, 0.80, 0.89$, and 0.96). Across all stations, the SU2 solver demonstrates excellent agreement with the experimental data, accurately capturing the localized suction peak near the leading edge on the upper surface, as well as the smooth chordwise pressure recovery toward the trailing edge.As the simulation evolves in physical time, the development of the downstream wake column directly influences the blade surface physics, bringing the computed pressure profiles into closer asymptotic agreement with the experimental data. Examining the spanwise trends, the suction peak intensifies significantly as the radial station moves outward toward the tip, reflecting the higher local dynamic pressure. At the inboard stations ($r/R = 0.50$ and 0.68), minor discrepancies are observable near the trailing edge, where the fine grid exhibits a slight oscillatory behavior, likely due to its capacity to resolve localized, transient shear instabilities that are artificially damped by the numerical diffusion of the coarse grid. At the outboard stations ($r/R = 0.89$ and 0.96), where transonic effects begin to emerge near the blade tip, both grids match the experimental suction peak exceptionally well, confirming that the sliding interface logic successfully preserves flux conservation without introducing numerical artifacts across the moving zone boundaries.

The unsteady flow solver demonstrates good predictive accuracy. Computed sectional surface pressure (C_p) distributions from mid-span to the blade tip, along with integrated global thrust coefficients (C_T), correlated strongly with experimental data in Figure 5. As the wake column fully developes over the successive azimuthal rotations, the surface pressure profiles asymptotically converge toward experimental values, validating the dual-time-stepping approach.

3.1 Mesh Sensitivity Analysis

To evaluate the influence of spatial discretization on the numerical solution, a mesh sensitivity study is conducted using two distinct grid resolutions for the Caradonna-Tung rotor blade case. The mesh characteristics and explicit element counts for both configurations are detailed in Table 2. The coarse mesh utilizes a chordwise spacing of $0.025c$ and a spanwise spacing of $0.06c$, yielding approximately 7,600 surface points on the blade. Refinement to the fine mesh reduces these grid spacings to $0.01c$ and $0.03c$ in the chordwise and spanwise directions, respectively, which quadruples the surface resolution to 29,470 points. This surface refinement correspondingly scales the volume mesh; the inflation layer's prism elements increase from 1.34 million to 5.2 million, while the far-field tetrahedral elements grow from

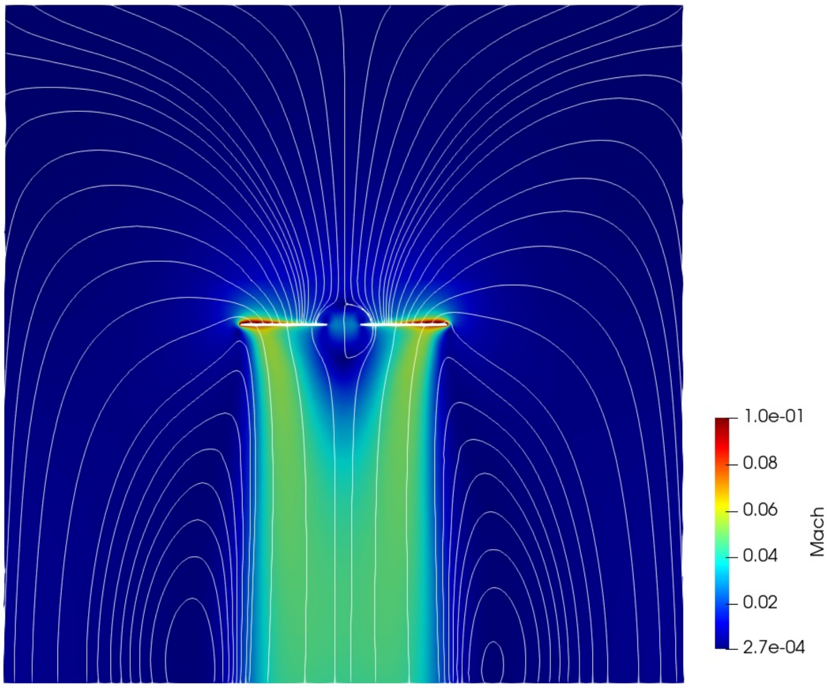

Figure 4: Mach number distribution

4.08 million to 14.3 million. Consequently, the total mesh density expands nearly fourfold, increasing from 5.43 million elements in the coarse baseline to 19.5 million elements in the fine grid configuration.

Table 2: Comparison of mesh resolution parameters and element counts for Caradonna Tung Case

Mesh Parameter	**Coarse Mesh**	**Fine Mesh**
Chordwise spacing	$0.025c$	$0.01c$
Spanwise spacing	$0.06c$	$0.03c$
Blade surface points	7,600	29,470
Prism elements	1.34 M	5.2 M
Tet elements	4.08 M	14.3 M
Total elements	**5.43 M**	**19.5 M**

To visually evaluate the spatial discretization, the grid topology for both configurations is illustrated at the blade surface and within the volume domains. Figure 6 contrasts the blade surface grids, clearly demonstrating the increased density achieved by tightening the chordwise and spanwise spacing on the fine grid. This surface refinement is further reflected in the off-body volume mesh.

As shown in the rotating grid block cut sections in Figure 7, both the coarse grid and fine grid configurations utilize structured prism layers adjacent to the solid boundaries to resolve the viscous boundary layer, transitioning into unstructured tetrahedral elements in the far-field. The fine grid configuration significantly clusters elements near the blade profiles and within the wake development regions, capturing the high-gradient flow physics with much greater fidelity than the baseline coarse mesh.

Figure 8 compares the nearbody (a) coarse and (b) fine grid topologies used for the mesh sensitivity study. Both configurations feature structured prism layers near the blade surface for boundary layer resolution, transitioning into an unstructured tetrahedral far-field. The coarse mesh (a) exhibits rapid cell expansion away from the wall with localized downstream refinement. In contrast, the fine mesh (b) implements a higher spatial resolution with a gradual volumetric growth rate around the entire nearbody block, reducing

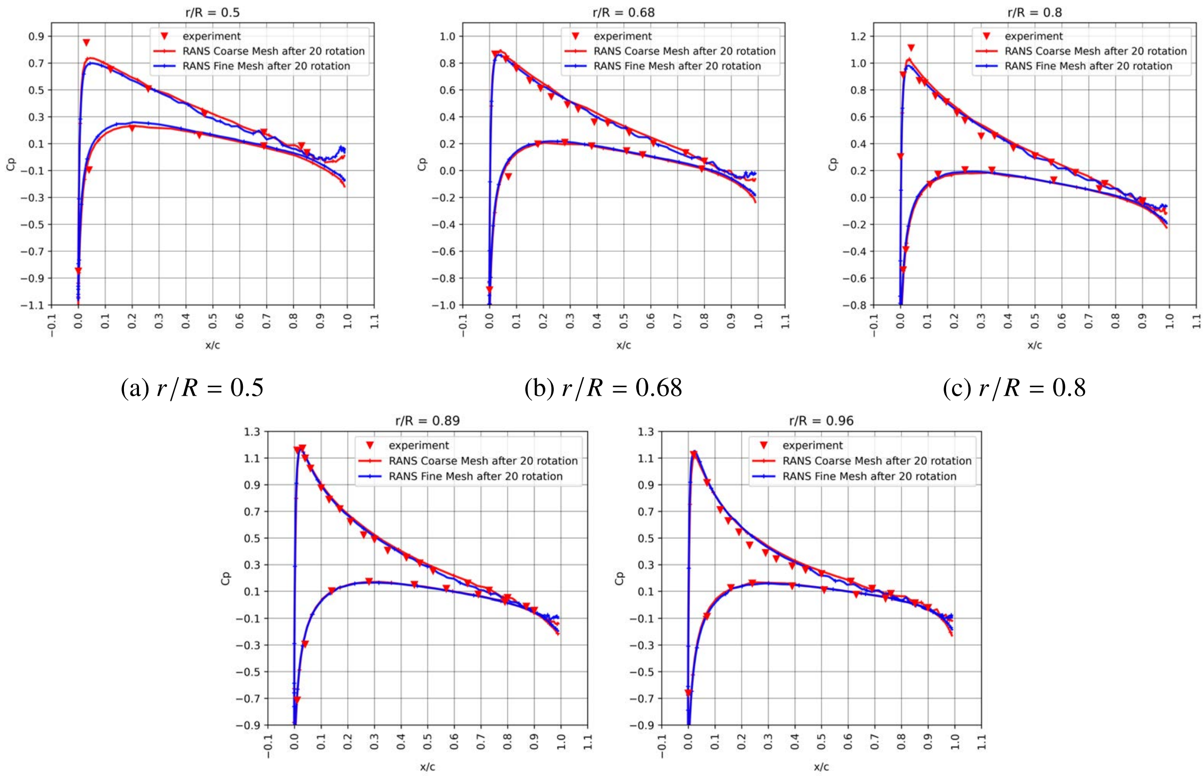

(a) $r/R = 0.5$ (b) $r/R = 0.68$ (c) $r/R = 0.8$

(d) $r/R = 0.89$ (e) $r/R = 0.96$

Figure 5: Surface pressure (C_p) distributions along the blade span at 1500 RPM, 8° collective.

numerical diffusion to better capture localized high-gradient flow structures.

The impact of spatial discretization on the blade loading characteristics is evaluated via the surface pressure contours presented in Figure 9. Both the coarse and fine grid configurations successfully predict the primary aerodynamic features of the rotor blade in hover, showing a distinct low-pressure region on the upper suction surface near the leading edge and a steady recovery toward the trailing edge. This localized suction peak intensifies moving radially outward toward the blade tips, capturing the expected spanwise increase in aerodynamic loading. While the global pressure patterns appear macroscopically similar between the two resolutions, a closer inspection reveals that the fine grid configuration yields smoother contour transitions and a more sharply defined suction expansion zone near the tip regions. Conversely, the coarse grid exhibits subtle spatial oscillations and slightly smeared pressure gradients along the suction peak, illustrating how localized grid refinement is essential for accurately isolating high-gradient expansions and tracking precise surface loading profiles.

The critical role of grid refinement in capturing wake dynamics is highlighted by the vorticity magnitude contours in Figure 9b. While both configurations identify the localized vorticity at the blade tips and roots, the wake resolution on the coarse grid (a) is severely degraded. High numerical diffusion on the coarse mesh rapidly dissipates and smears the shear layers immediately below the rotor plane, obscuring the downstream wake structure. Conversely, the fine grid (b) yields less numerical dissipation, sharply resolving the concentrated, high-gradient vortex cores much further downstream and capturing the wavy shear layer instabilities along the slipstream boundary. Consequently, the simulation evolution is not identical between the two cases, as the fine grid alters the development and settling of these unsteady flow features over time. However, despite these structural improvements, the fine grid resolution remains insufficient to completely resolve and preserve the tip vortices without decay as they propagate deeper into the far-field wake, indicating the need for further localized refinement or advanced wake-capturing methods.

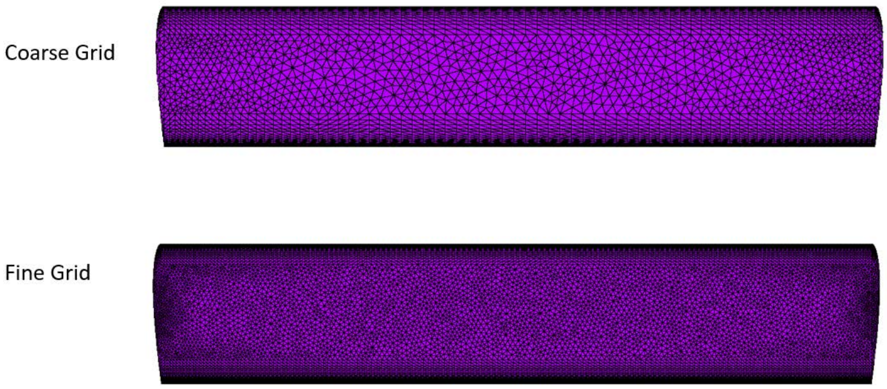

Figure 6: Blade Surface Grids

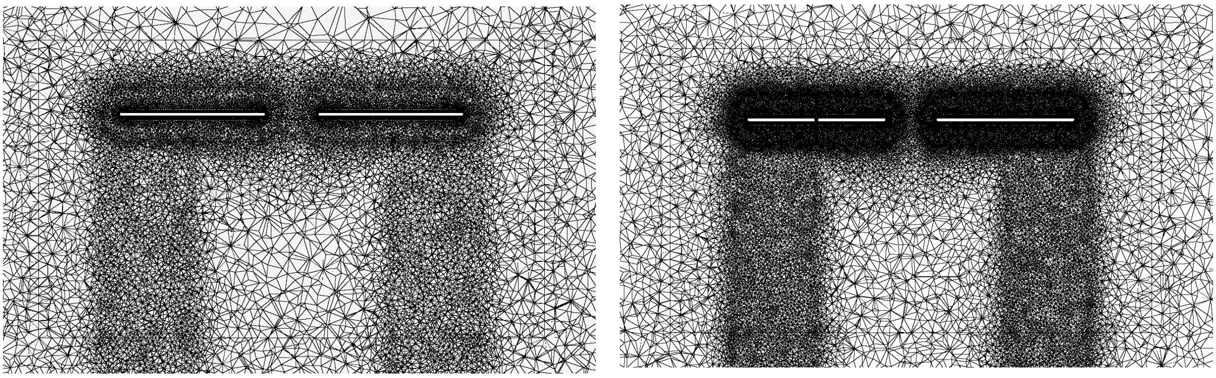

(a) Coarse Grid (b) Fine Grid

Figure 7: Close-up view of the rotating grid blocks

The integrated rotor performance metrics further confirm the predictive capability of the computational framework. The experimental thrust for this case is reportable as 735 N, corresponding to a thrust coefficient (C_T) of 0.00455 [1]. On the coarse grid, the solver predicts a physical thrust of 820 N (C_T = 0.00498), overestimating the total aerodynamic load due to the higher numerical diffusion and coarser resolution near the blade boundaries. Refinement to the fine grid significantly improves the accuracy of the integrated loads; the calculated thrust drops to 761 N (C_T = 0.00463), bringing the numerical solution into much closer agreement with the experimental measurements and confirming the convergence trend of the unsteady flow solver.

A key focus is to contrast a 5.43 million element coarse grid with a refined 19.5 million element fine grid to evaluate spatial discretization impacts on high-gradient flow features. The quantitative comparison across configurations is summarized in Table 3.

Despite major spatial improvements, the fine grid is still insufficient to track tip vortices into the deep far-field without eventual decay. This highlights a persistent challenge in capturing long-term rotor wake conservation via traditional grid refinement alone.

High-fidelity, unsteady aerodynamic simulations of the Caradonna-Tung rotor in hover are successfully validated using the open-source SU2 suite. To isolate the performance of the unsteady RANS solver and the sliding grid structure, the blade is assumed rigid. The computational strategy utilized a multi-block hybrid grid layout with a sliding interface zone to capture the rotational motion.

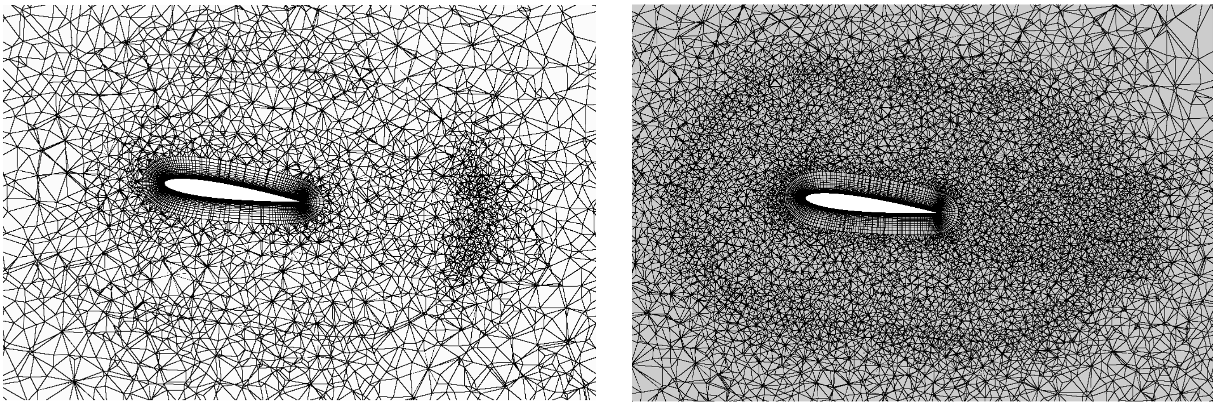

(a) Coarse Grid (b) Fine Grid

Figure 8: Close-up view of the grid blocks around blades

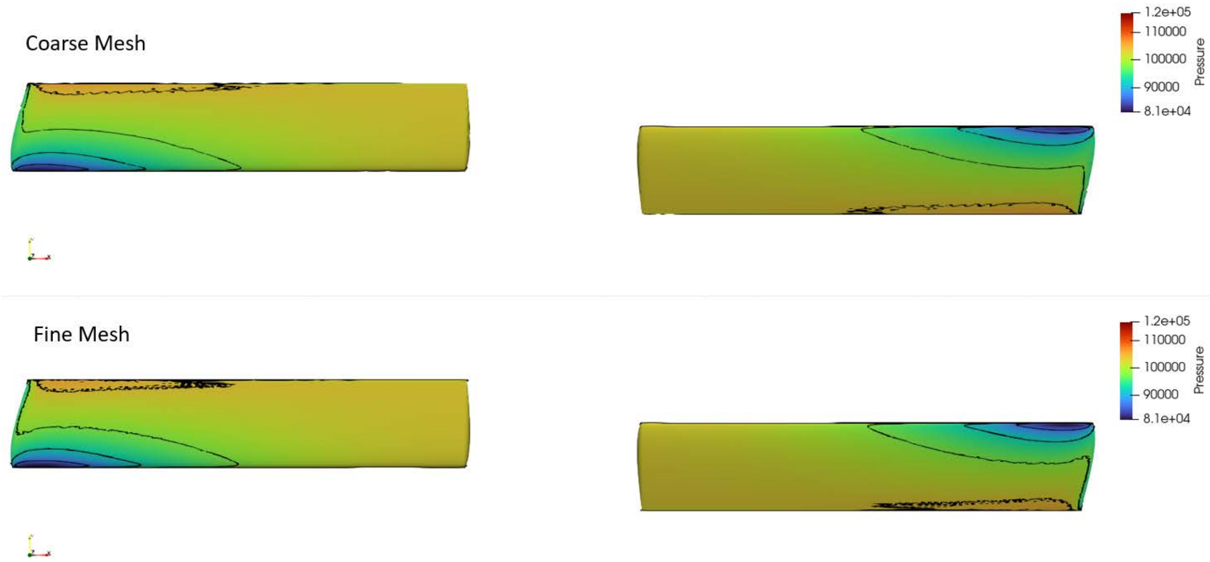

Figure 9: Blade surface pressure distributions

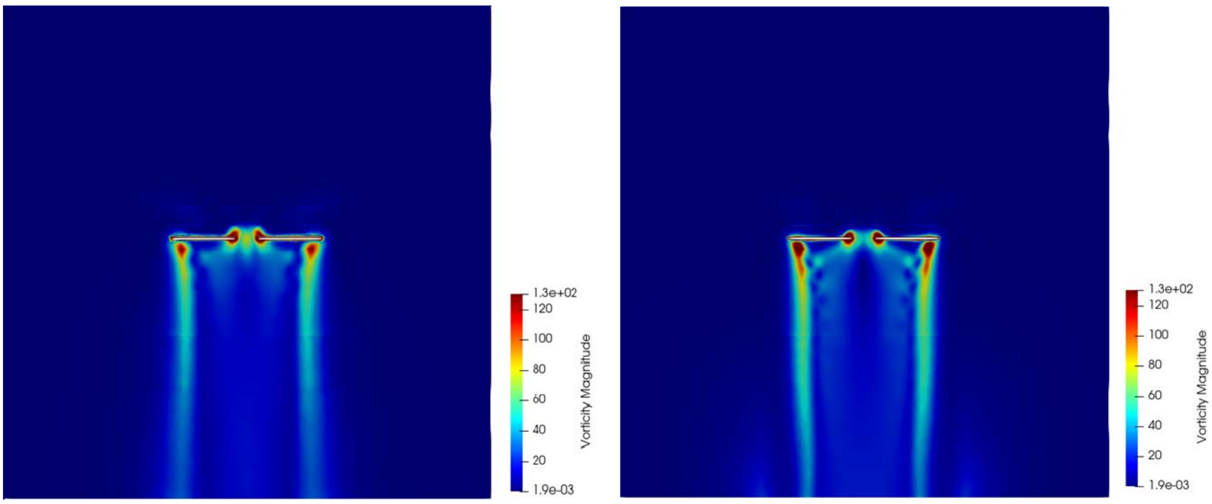

(a) Coarse Grid (b) Fine Grid

Figure 10: Vorticity distributions at 1500 RPM and 8° collective pitch.

Table 3: Quantitative and Qualitative Mesh Sensitivity Performance Metrics.

Metric	Coarse Grid (5.43M)	Fine Grid (19.5M)	Experimental Baseline
Thrust, F (N)	820 N	761 N	735 N
Thrust Coeff., C_T	0.00498	0.00468	0.00455
Flow Features	High numerical diffusion; unphysically dissipated tip vortices and smeared shear layers.	Mitigated artificial dissipation; resolved concentrated vortex cores and wavy shear layer instabilities.	Baseline reference

4. Conclusion

The strong agreement between the current numerical framework and established literature confirms that the SU2 transient flow solver, nested block-mesh refinement zones, and sliding interface boundary conditions are highly accurate. While spatial discretization heavily influences the resolution of high-gradient tip vortices, the refined 19.5 million element mesh successfully minimized artificial dissipation, bringing global thrust predictions into close alignment with experimental data. The specialized near-body blocks surrounding the blade surfaces are now thoroughly verified in their rigid state. This completed baseline validation yields the essential, verified foundation required to confidently progress to high-fidelity, fully coupled Fluid-Structure Interaction (FSI) simulations. Future work will remove the rigid constraint to incorporate deforming mesh blocks and flexible multibody dynamics for comprehensive aeroelastic analysis.

5. Acknowledgement

High-fidelity unsteady simulations are performed on the TÜBİTAK TRUBA high-performance computing (HPC) infrastructure utilizing the ARF cluster.

References

[1] F. X. Caradonna and C. Tung. Experimental and analytical studies of a model helicopter rotor in hover. *NASA Technical Memorandum*, (TM-81232), 1981.

[2] J. Gordon Leishman. *Principles of Helicopter Aerodynamics*. Cambridge University Press, 2nd edition, 2006.

[3] Richard L. Bielawa. *Rotary Wing Structural Dynamics and Aeroelasticity*. AIAA Education Series, 2nd edition, 2006.

[4] Wayne Johnson. *Rotorcraft Aeromechanics*. Cambridge University Press, 2013.

[5] Olivier A. Bauchau. *Flexible Multibody Dynamics*, volume 176. Springer Science & Business Media, 2011.

[6] Wayne Johnson. A comprehensive analytical model of rotorcraft aerodynamics and dynamics (CAMRAD). Part 1: Theory manual, Part 2: User's manual. Technical Report NASA TM-81280 and TM-81281, NASA Ames Research Center, Moffett Field, California, June 1981.

[7] J. Gordon Leishman and Thomas S. Beddoes. A semi-empirical model for dynamic stall. *Journal of the American Helicopter Society*, 34(3):3–17, July 1989.

[8] Francis X. Caradonna and Chee Tung. Experimental and analytical studies of a model helicopter rotor in hover. Technical Report NASA TM-81232, NASA Ames Research Center, 1981.

[9] Mark Potsdam, Hyeonsoo Yeo, and Wayne Johnson. Rotor aeroelastic analysis using CFD coupled with a comprehensive code. *AHS International Journal*, 49(4):74–81, 2004.

[10] Anubhav Datta, Hyeonsoo Yeo, and Inderjit Chopra. Rotor CFD/CSD coupled analysis for acceleration and vibration predictions. *Journal of the American Helicopter Society*, 51(4):333–346, October

2006.

[11] Francisco Palacios, Michael R. Colonno, Aniket C. Aranake, Alejandro Campos, Sean R. Copeland, Thomas D. Economon, Amrita K. Lonkar, Trent W. Lukaczyk, Thomas W. R. Taylor, and Juan J. Alonso. Stanford university unstructured (SU2): An open-source integrated computational environment for multi-physics simulation and design. In *51st AIAA Aerospace Sciences Meeting including the New Horizons Forum and Aerospace Exposition*, pages AIAA 2013–0287, 2013.

[12] Thomas D. Economon, Francisco Palacios, Sean R. Copeland, Trent W. Lukaczyk, and Juan J. Alonso. SU2: An open-source suite for multiphysics simulation and design. *AIAA Journal*, 54(3):828–846, 2016.

[13] Philippe R. Spalart and Steven R. Allmaras. A one-equation turbulence model for aerodynamic flows. *AIAA Paper*, 439:1992, 1992.

[14] Philip L. Roe. Approximate riemann solvers, parameter vectors, and difference schemes. *Journal of Computational Physics*, 43(2):357–372, 1981.

[15] Antony Jameson. Time dependent applications of Any Method of Convergence Acceleration vs. Steady State. In *10th Computational Fluid Dynamics Conference*, pages AIAA Paper 1991–1596, June 1991.

[16] Piotr Doerffer and Oskar Szulc. Numerical simulation of model helicopter rotor in hover. *Task Quarterly*, 12(3):227–236, 2008.